PROCEEDINGS PAPER

Energy-dispersive diffraction tomography of shark vertebral centra

Jun-Sang Park,[1] Ryan M. Horn,[2] Haiyan Chen,[3] Kelsey C. James,[4] Michelle S. Passerotti,[5] Lisa J. Natanson,[5,*] and Stuart R. Stock [6,a)]
[1]*Advanced Photon Source, Argonne National Laboratory, Lemont, IL, USA*
[2]*Department of Aerospace Engineering, Purdue University, West Lafayette, IN, USA*
[3]*Mineral Physics Institute, Stony Brook University, Stony Brook, NY, USA*
[4]*SW Fisheries Science Center, National Marine Fisheries Service, NOAA, La Jolla, CA, USA*
[5]*NE Fisheries Science Center, National Marine Fisheries Service, NOAA, Narragansett, RI, USA*
[6]*Department of Cell and Developmental Biology, Feinberg School of Medicine, and Simpson-Querrey Inst., Northwestern Univ., Chicago, IL, USA*

(Received 12 March 2024; accepted 4 April 2024)

Shark vertebrae and their centra (vertebral bodies) are high-performance structures able to survive millions of cycles of high amplitude strain despite lacking a repair mechanism for accumulating damage. Shark centra consist of mineralized cartilage, a biocomposite of bioapatite (bAp), and collagen, and the nanocrystalline bAp's contribution to functionality remains largely uninvestigated. Using the multiple detector energy-dispersive diffraction (EDD) system at 6-BM-B, the Advanced Photon Source, and 3D tomographic sampling, the 3D functionality of entire centra were probed. Immersion in ethanol vs phosphate-buffered saline produces only small changes in bAp *d*-spacing within a great hammerhead centrum. EDD mapping under *in situ* loading was performed an entire blue shark centrum, and 3D maps of bAp strain showed the two structural zones of the centrum, the corpus calcareum and intermedialia, contained opposite-signed strains approaching 0.5%, and application of ~8% nominal strain did not alter these strain magnitudes and their spatial distribution.

[doi:10.1017/S0885715624000307]

Key words: shark, vertebral centrum, bioapatite, energy-dispersive diffraction, tomography, synchrotron X-radiation

I. INTRODUCTION

Sharks have vertebrae whose centra (vertebral bodies) consist of cartilage, the centra of many species are mineralized with nanoplatelets of a bioapatite (bAp), a form of hydroxyapatite related to that in bone (Urist, 1961; Dean et al., 2005; Park et al., 2022a), and the bAp crystallographic *c*-axes are oriented parallel to the cartilage fibril axes. Note that in load bearing tissues such as the long bones, the cartilage fibril and bAp *c*-axes are parallel to the axis of principal strain (Martin et al., 1998).

The centra of shark abdominal vertebrae carry the *in vivo* loads generated during swimming (Porter and Long, 2010). Shark centra experience tens of millions of cycles of swimming-related loading (Watanabe et al., 2012), and this loading alternates compression of the left side of the centra with compression of the right side. Strain magnitudes can reach 3–8% (Porter et al., 2014), an enormous level for mineralized tissue, especially considering that the centra do not appear to have a remodeling mechanism like that in bone for replacing portions that have accumulated microdamage.

Shark centra have complex 3D structures consisting of an hourglass-shaped double cone of mineralized cartilage (Figure 1) termed the corpus calcareum and of the mineralized cartilage of the intermedialia which lies between and supports the rostral and caudal cone walls. In the carcharhiniforms, which include the great hammerhead and blue sharks, the subjects of this report, the intermedialia consist of four wedges

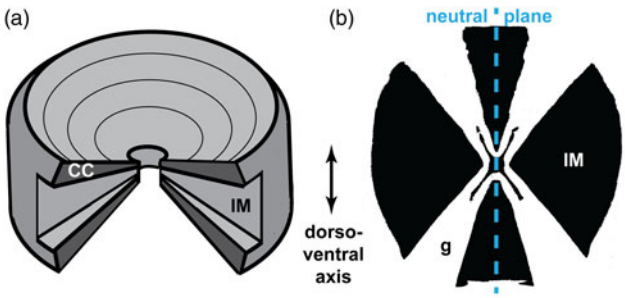

Figure 1. Schematic of a carcharhiniform shark centrum. (a) 3D schematic with a sector removed to show the internal structure. The double cone of the corpus calcareum "CC" and the wedges of the intermediale "IM" are labeled as is the shark's dorso-ventral axis. (b) Schematic cross-section through the middle of the centrum showing the unmineralized regions "g" between the four mineralized wedges of the intermedialia. The cyan dashed line is the bending neutral plane.

* (retired).
[a)]Author to whom correspondence should be addressed. Electronic mail: s-stock@northwestern.edu

separated with non-mineralized tissue (Figure 1). A fluid-filled intervertebral capsule lies between the cone walls of adjacent vertebrae.

Data on shark centra macro-, micro-, and nanostructure are sparse, but recent studies are filling in the gaps. Morse et al. (2022) studied the 3D macrostructure of multiple species' centra using microComputed Tomography (microCT) with volume elements (voxels) > 15 μm and found that all carcharhiniform centra studied had higher mineral levels in the corpora than in the intermedialia. Stock et al. (2022) showed a small amount of synchrotron microCT data showing the centra tissue consists of fine trabeculae separated by unmineralized space. Park et al. (2022a) found bAp lattice parameters and crystallite size values slightly different from those typical of mammalian bone. Finally, a novel approach, energy-dispersive diffraction (EDD) with the unique multi-detector system at beamline 6-BM-B, Advanced Photon Source (APS), was used to map the 3D spatial variation of diffracted intensity and its variation with anatomical orientation (Park et al., 2022b).

The study reported below employed EDD at 6-BM-B, APS, and a simple loading apparatus to examine the magnitude and spatial distribution of strains within a blue shark centrum. Preliminary strain maps for different deformations applied to the blue shark centrum were measured and related to the centrum's anatomy. The mapping experiments required many hours of data collection, and the centrum was immersed in 50% ethanol to prevent drying and biological degradation. The effect of immersion in 50% ethanol vs immersion in more natural phosphate-buffered saline (PBS) was also studied by mapping one half of a great hammerhead centrum in the former and the second half in the latter.

II. MATERIALS AND METHODS

One abdominal centrum of an adult blue shark (*Prionace glauca*, from vertebra numbers 81–84) was used for the *in situ* loading experiments. An abdominal centrum of an adult great hammerhead shark (*Sphyrna mokarran*) was cut along its dorso-ventral midline (i.e., along the neutral plane indicated in Figure 1(b), that is radially through the two smaller wedges). One half was used for immersion in 50% ethanol (EtOH) and one half in PBS. The specimens were obtained under National Marine Fisheries Service, Highly Migratory Species Management Division Exempted Fishing Permit Number SHK-EFP-19-02.

Energy-dispersive diffraction employs a polychromatic beam, and, for a polycrystalline sample, properly aligned crystallites diffract X-rays with different energies. In the transmission geometry, a microbeam is typically defined with an incident beam collimator (Figure 2(a)), and a receiving slit at angle 2θ from the incident beam is used to isolate the volume whose diffracted intensity is to be measured. An energy-sensitive detector or detectors measure the energies of the diffraction peaks which are then converted into d-spacings $d_{hk.l}$ for lattice planes $hk.l$ (Here the abbreviated Miller–Bravais indexing system is used to emphasize the hexagonal crystal system of bAp) via Bragg's law, $\lambda = 2\, d_{hk.l} \sin\theta$, where θ is the Bragg angle and is defined by the receiving slit and λ is

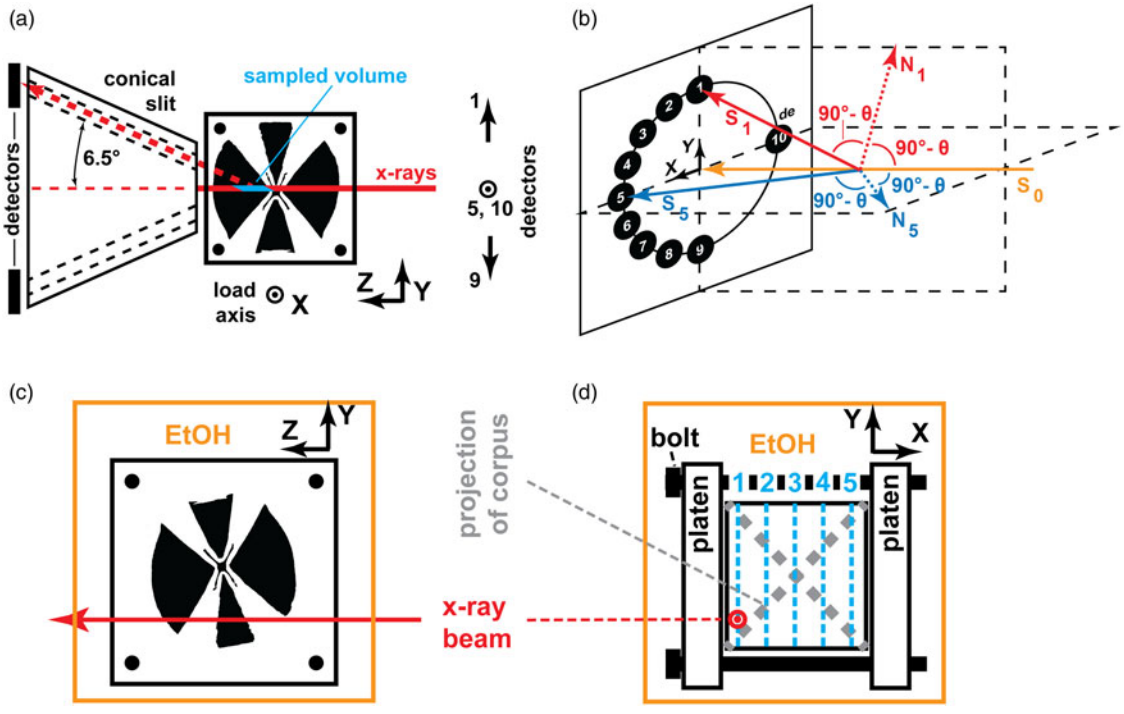

Figure 2. (a) Schematic of the 6-BM-B apparatus with load frame observed from the side (along the horizontal laboratory axis X which is perpendicular to the incident beam direction Z). The incident X-ray beam is indicated by the solid red line, one of the diffracted beams by the dashed red line and the sampled volume by the cyan parallelopiped. The load axis is parallel to X, and the sampled diffraction beam directions for detectors 1, 5, 9, and 10 are shown schematically at the right of this panel. (b) This schematic illustrates the bAp nanocrystal orientations (normals N_1 and N_5) and diffracted beam direction (S_1 and S_5, respectively) sampled by detectors 1 (red) and 5 (blue), respectively. The orange line is the incident beam direction S_0. (c) Schematic of the load frame (Z–Y plane) in the plastic container filled with 50% EtOH. The incident beam direction is shown in red. (d) Y–Z mapping planes 1–5 indicated by the dashed cyan lines. The projection of the centrum's corpus is shown by the dashed gray bars.

https://doi.org/10.1017/S0885715624000307 Published online by Cambridge University Press

the measured wavelength of the diffraction peak. Mapping is performed by simple translations.

The centrum measurements described in this paper were performed using the multi-detector system of beamline 6-BM-B, APS, which is described elsewhere (Weidner et al., 2010). A collimator formed a pencil beam of polychromatic radiation which passed through the specimen along direction Z (Figure 2(a), a schematic transverse section near the middle of a carcharhiniform centrum). The beam dimensions were 0.2×0.2 mm^2 for the great hammerhead centrum and 0.1×0.1 mm^2 for the blue shark centrum. The conical receiving slits block all radiation except that diffracted from the sampled volume at an angle $2\theta = 6.5°$ (Figure 2(a)), and the length of the sampling volume along Z was about 1.7 mm. Figure 2(b) shows the arrangement of the 10 energy-sensitive detectors of the 6-BM-B instrument. The schematic at the right side of Figure 2(a) shows the sampling directions of two pairs of detectors: detectors 1 and 9 measured intensities from bAp nanocrystals oriented to diffract along the vertical direction Y, and detectors 5 and 10 observed bAp nanocrystals diffracting along horizontal direction X. Each centrum (with or without the load frame) was fixed in place within a thin-walled plastic container filled with fluid.

Each great hammerhead hemi-centrum was mounted in the plastic container filled with either 50% EtOH or PBS. The incident beam direction Z was along the vertebral column axis, so that a rectangular scan area would minimize sampling of the fluid. Diffraction patterns with 40 s integration were recorded from a single X–Z plane with sampling at 56 points along X (with spacing $\Delta X = 0.2$ mm) and 11 points along Z (with spacing $\Delta Z = 1.5$ mm). Most of the 616 patterns were within the intermediale, but a fraction sampled fluid outside the centrum. Intensities for three reflections were strong enough for measurement of d: 00.2, the unresolved 21.1 + 11.2 + 0.30 + 20.2 quadruplet reflection and 13.0.

Figure 2(a) shows the load frame as oriented in the 6-BM-B instrument for the blue shark centrum study; the load axis was parallel to X. After mapping state 0 (both platens in contact with the faces of the centrum but with only enough compression to hold the centrum in place), the platen separation ΔX_{platen} was decreased two times (Table I) by tightening the bolts at the corners of the load frame. Note that the load frame was removed and replaced after each deformation increment, and the X positions for subsequent maps were determined after observing the positions of the platen in the radiography mode of the instrument. Linear translators moved the centrum across the sampling volume along the three orthogonal axes X (horizontal, perpendicular to the incident beam), Y (vertical, perpendicular to the incident beam), and Z (horizontal, parallel to the incident beam). The translation range and number of equally spaced positions were 25 mm and 19 positions for Y and 23 mm and 21 positions for Z. Five Y–Z planes were recorded at the X positions given in Table I. Exposure time was 30 s per pattern.

Strains were calculated for the quadruplet reflections at each point X,Y,Z where the diffracted intensity (sum of all ten detectors) was greater than 10% of the maximum in that map. Strain was defined as $(d_{obs}–d_0)/d_0$, where d_{obs} is the observed d-spacing for a given detector and d_0 is the mean d-spacing observed in each map of the same detector at state 0. In this preliminary report, only maps for detectors 1 and 5 are reported at two states (states 0 and 2) and at three X positions (1, 3, and 5).

III. RESULTS

Figure 3 compares mean values of $d_{00.2}$, d_{quad}, and $d_{13.0}$ as a function of detector number for the great hammerhead hemicentra in EtOH and in PBS. The mean values in EtOH are always larger than those in PBS, but the difference is typically on the order of 0.1% for $d_{00.2}$ and slightly larger for d_{quad} and $d_{13.0}$. The standard deviation of $d_{00.2}$ is about the same size as the EtOH-PBS difference, but those for d_{quad} and $d_{13.0}$ are somewhat larger.

Figure 4 shows quadruplet strain maps for EDD slice $X1$: Figure 4(a) shows strain state 0 for detector 1 (left) and detector 5 (right); Figure 4(b) shows strain state 2 for detector 1 (left) and detector 5 (right); Figure 4(c) shows a slice from laboratory microCT (absorption contrast) at a position corresponding to EDD slice $X1$. As expected for the position of $X1$ near the plastic platen, a ring of high measurable intensity is observed around a central area producing no diffraction. Around the ring at both states 0 and 2, the two to four o'clock and eight to ten o'clock positions have relatively large positive detector 1 strains (approaching 5×10^{-3}) and mostly large negative detector 5 strains (approaching -5×10^{-3}); anatomically, these orientations are along the medio-lateral axes of the centrum. The positions between ten and two o'clock were largely uncovered in slice $X1$, and the four to eight o'clock sector was only partially covered. Where data were collected in these dorso-ventral sectors, the detector 1 and 5 strains were mixed between near zero values and areas of large negative strain.

In slice $X1$, some slight changes were observed in going from state 0 to state 2. In the left-hand column of the maps (cyan arrows), for example, detector 1 strains decreased in magnitude (became less positive), and the detector 5 strain also became more positive. The orange arrows indicate positions where the strains became more positive. For example, within the eight to ten o'clock sector, the detector 1 strains within the second and third columns become slightly more positive in going from state 0 to state 2, and the detector 5

TABLE I. Platen separation ΔX_{platen}, X positions where YZ maps were recorded, and translation increments ΔY and ΔZ.

		X positions scanned						
State	ΔX_{platen}	1	2	3	4	5	ΔY	ΔZ
0	11.1	**−3.00**	−1.11	**0.78**	2.67	**4.56**	1.12	1.33
1	10.6	−3.30	−1.41	0.48	2.37	4.26	1.01	1.33
2	10.3	**−5.90**	−4.01	**−2.12**	-0.23	**1.66**	1.05	1.33

Units are millimeters throughout. Only the X positions and states shown in bold are reported in this paper.

https://doi.org/10.1017/S0885715624000307 Published online by Cambridge University Press

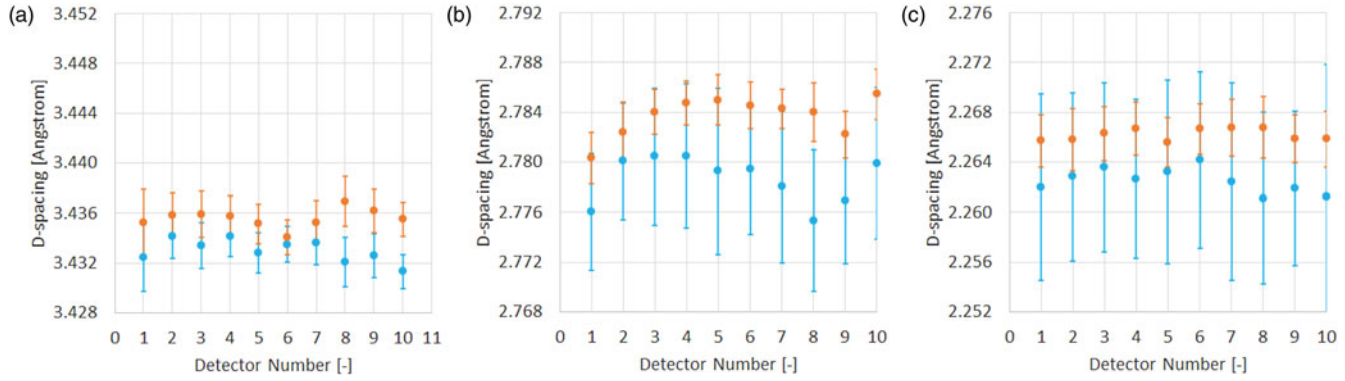

Figure 3. Plots of mean *d*-spacing in PBS (cyan) and in EtOH (orange) as a function of detector number for (a) 00.2, (b) the quadruplet reflection, and (c) 13.0. The mean is for 287 positions in each great hammerhead hemi-centrum, and the scatter bars give the standard deviations.

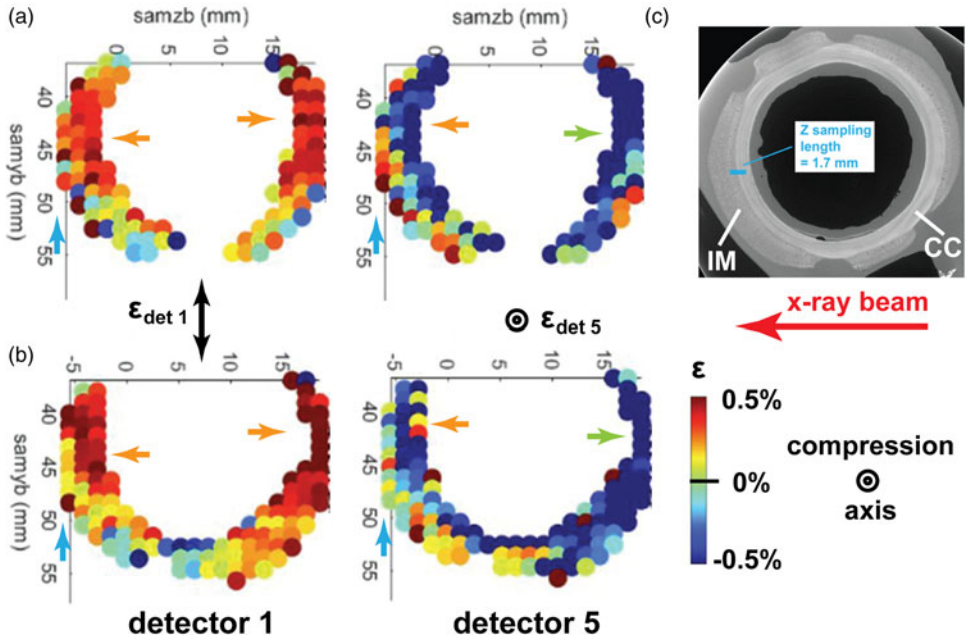

Figure 4. Strain (quadruplet reflection) within EDD slice *X*1 which contains primarily corpus material. (a) State 0 strains for detector 1 (left) and detector 5 (right). (b) State 2 strains for detector 1 (left) and detector 5 (right). (c) Absorption microCT slice with lighter pixels signifying greater mineral content, from Morse et al. (2022). The color bar gives the strain scale and the arrowed lines the various directions: X-ray beam direction, compression axis, and strain directions measured by detectors 1 and 5. The small cyan, green, and orange arrows are identified in the text. The directions of the detector 1 and detector 5 strains are given by $\epsilon_{\text{det 1}}$ and $\epsilon_{\text{det 5}}$, respectively. The *Z* and *Y* axes are labeled samzb and samyb, respectively.

strains within the third column also became more positive. Within the two to four o'clock sector, detector 1 strains increased from state 0 to 2, but for detector 5 (green arrows) the strains at these positions did not change (i.e., they remained at the maximum negative values).

Figure 5 shows quadruplet strain maps for EDD slice *X*3: Figure 5(a) shows strain state 0 for detector 1 (left) and detector 5 (right); Figure 5(b) shows strain state 2 for detector 1 (left) and detector 5 (right); Figure 5(c) shows a slice from laboratory microCT (absorption contrast) at a position corresponding to EDD slice *X*3. The four wedges of the intermediale are well-defined and are separated by unmineralized gaps U. At the position of *X*3, the corpus is a narrow ring of contrasting strain state near the center of the map and surrounding a small volume without diffracted intensity. For the intermedialia, the detector 1 strains are primarily negative and large (approaching -5×10^{-3}), and these strains do not appear to change appreciably upon going from state 0 to state 2. The detector 5 strains for the intermedialia, however, have the opposite sign and can reach large positive values (approaching 5×10^{-3}) near the perimeter of the large wedges. The detector 5 strains do not appear to change significantly between state 0 and state 2. In all cases, the corpus strains are of the opposite sign to those in the intermedialia and have the maximum magnitudes observed (approaching $\pm 5 \times 10^{-3}$); the corpus strains do not appear to change appreciably between state 0 and state 2.

Figure 6 shows maps for *X*5; this cross-section is on the opposite side of the midplane of the centrum. Somewhat more corpus material and somewhat less intermedialia material is present in cross-section *X*5 than in *X*3, but the same trends are present in both of these cross-sections. Specifically, detector 1 and 5 strains have the opposite sign as do the corpus and intermediale in maps for a single detector.

https://doi.org/10.1017/S0885715624000307 Published online by Cambridge University Press

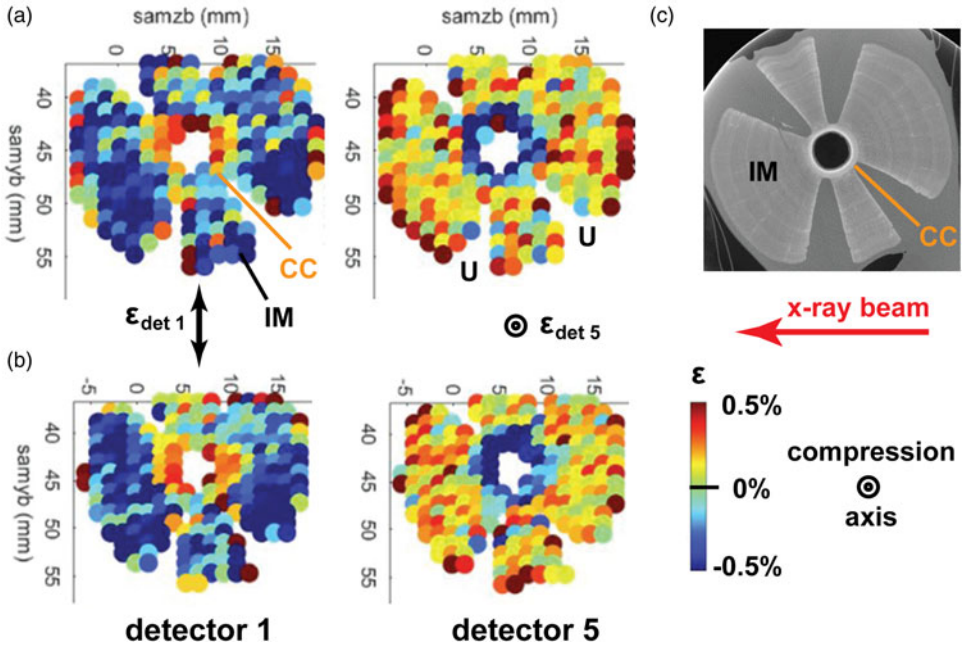

Figure 5. Strain (quadruplet reflection) within EDD slice *X*3 which contains intermedialia (IM) and corpus (CC) material. The corpus material is the narrow ring at the center, and the intermedialia of contrasting colors surrounds the corpus. Note the unmineralized gaps between the wedges of the intermedialia, two of which are labeled U. (a) State 0 strains for detector 1 (left) and detector 5 (right). (b) State 2 strains for detector 1 (left) and detector 5 (right). (c) Absorption microCT slice from Morse et al. (2022). The other symbols are the same as in Figure 4.

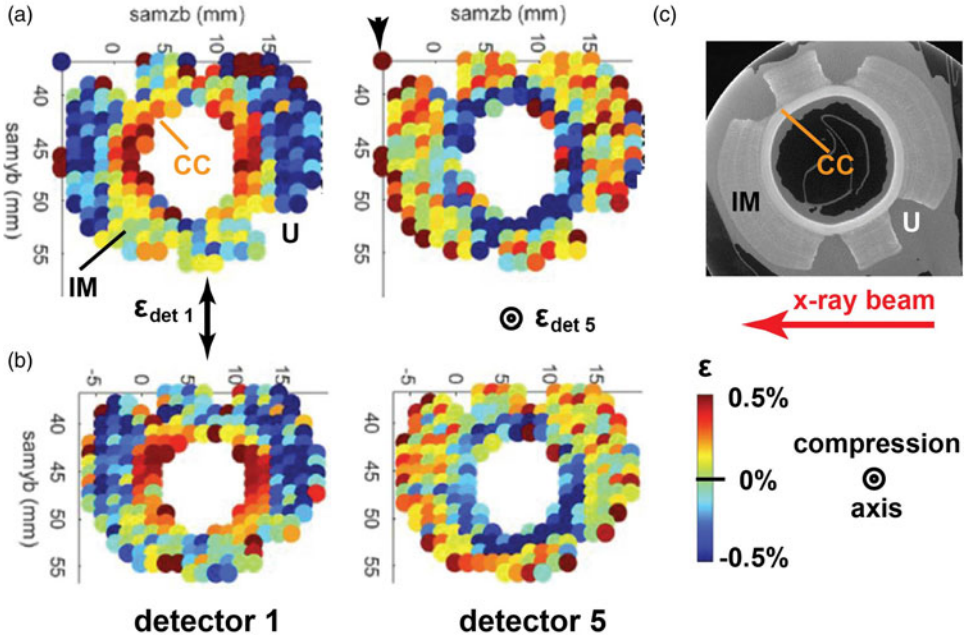

Figure 6. Strain (quadruplet reflection) within EDD slice *X*5 which contains intermedialia (IM) and corpus (CC) material. The corpus material is the narrow ring at the center, and the intermedialia of contrasting colors surrounds the corpus. Note the unmineralized gaps between the wedges of the intermedialia, one of which is labeled U. (a) State 0 strains for detector 1 (left) and detector 5 (right). (b) State 2 strains for detector 1 (left) and detector 5 (right). (c) Absorption microCT slice from Morse et al. (2022). The other symbols are the same as in Figure 4.

There is not much change in strains between state 0 and state 2, similar to what is seen for *X*1 and *X*3.

IV. DISCUSSION

Figure 3 shows that the bAp quadruplet *d*-spacing for the different detectors is distributed about ~2.780 Å. The difference in *d*-spacing in PBS relative to EtOH is $\Delta d_{\text{PBS-EtOH}}$ ~0.004 Å; the strain produced by EtOH immersion is about 0.14%, substantially smaller than the strains plotted in Figures 4–6. The strains observed in the blue shark centrum are, therefore, intrinsic to the specimen and not to EtOH. Further, the difference between mean *d*-spacing in EtOH and PBS is slightly greater than the standard deviation

https://doi.org/10.1017/S0885715624000307 Published online by Cambridge University Press

of the *d*-spacings, so the interpretation of quadruplet strain differences less than 0.1% is problematic within the maps of Figures 4–6.

The bAp quadruplet strain maps at state 0 (Figures 4–6) have large positive and negative values of magnitude 0.5%, despite the fact that there is essentially zero applied compressive displacement. This suggests that the strains are residual strains, that is, strains grown into the structure or developed over many loading cycles. The centrum consists of bAp nanocrystallites (Park et al., 2022a) embedded in a matrix of cartilage, and it is not unreasonable to suppose that, like what is seen in bone (Almer and Stock, 2005, 2007), the cartilage matrix is imposing this strain on the bAp phase. Alternatively, the differences in strain may reflect spatially distributed differences in bAp lattice parameter and hence composition; typically this would result from differences in carbonate concentration impurities. However, detector 1 and 5 data (the former along the dorso-ventral axis and the latter along the vertebral column axis) differ in the opposite directions, and this is a strong indication that the observed maps result from residual strains and not from composition variation.

The strains within the centrum always have the opposite sign from those in the intermedialia. This suggests that either *in situ* loading has induced opposite-signed residual stresses in the two structures or, as the centrum grows, the forming bAp responds to the continuous, *in vivo* straining and "builds in" residual strains. The difference between corpus and intermedialia residual strains is consistent with the observations of Park et al. (2022b) who found that bAp *c*-axis crystallographic differed between corpus and intermedialia. The question which remains is whether the differences are imposed by loading or they develop to resist the loading.

Only the most minor changes in the strain maps were observed in going from state 0 to 2. The difference in plate displacement between states 0 and 2 was 0.8 mm which corresponds to a nominal strain of ~8%. It is possible that the structure and its cartilage matrix are deforming without loading the bAp; this is not unreasonable given that synthetic hydroxyapatite particles embedded in a macromolecule matrix of a scaffold did not carry load, even when compressed to comparable strains (Stock et al., 2021). Stock et al. (2022) observed that the shark centrum consists of fine trabeculae on the order of 5–10 μm thickness separated by soft tissue spaces; local deflections and rotations of the trabeculae may also shield the bAp phase from being loaded. Another possibility for the small response of bAp in the bulk of the centrum is that all of the deformation is concentrated within the immediate vicinity of the two platens. The small differences noted in slice *X*1, closest to a platen, between states 0 and 2 might reflect this, but also might simply be limited in precision.

More replicates of this species and, in fact, of other species need to be studied to gain a more robust understanding of centrum response to deformation. This will not be a rapid process, first, because the mapping experiments are so slow (nearly 24 h of beam time are required to map a single deformation state with the resolution used here) and, second, because the 6-BM detector is unique and one cannot use multiple beamlines. Diffraction tomography for monochromatic X-rays could be used, e.g., Stock et al. (2008), but it remains to be determined whether this approach might provide appreciable, if any gain in throughput.

The simple compression loading experiments described here certainly do not reflect swimming-induced deformation which consists of compression on the left side of the centrum followed by compression of the right side of the centrum. In future experiments, this might be accomplished with the present apparatus by tightening the pair of bolts to either side of a wide wedge. The present experiments also do not recapitulate the *in vivo* boundary conditions: the presence of the fluid-filled intervertebral capsule between each pair of centra. One expects that that the capsule volume remains constant (incompressible fluid) but its shape can change up to a point, perhaps contributing variable stiffness to the structure. The present loading scheme may produce differential collapse of the cones near the platen, so a better way of mimicking *in vivo* loading is needed, perhaps by increasing the size of the container for the fluid and loading a set of contiguous vertebrae with intact and fluid-filled intervertebral capsules. Finally, one could incorporate a load cell.

Despite the limitations noted above, EDD mapping of strain distributions in an intact shark centrum under applied compression has provided new insights into this structure's functionality. Further, such investigation will doubtlessly provide additional valuable quantitative information.

ACKNOWLEDGEMENTS

This research used resources of the Advanced Photon Source, a U.S. Department of Energy (DOE) Office of Science User Facility, operated for the DOE Office of Science by Argonne National Laboratory under Contract No. DE-AC02-06CH11357. Argonne National Laboratory's work was supported by the U.S. Department of Energy, Office of Science, Office of Basic Energy Sciences, under contract DE-AC02-06CH11357.

REFERENCES

Almer, J. D., and S. R. Stock. 2005. "Internal Strains and Stresses Measured in Cortical Bone via High-Energy X-Ray Diffraction." *Journal of Structural Biology* 152: 14–27.

Almer, J. D., and S. R. Stock. 2007. "Micromechanical Response of Mineral and Collagen Phases in Bone." *Journal of Structural Biology* 157: 365–370.

Dean, M. N., W.-A. Chiou, and A. P. Summers. 2005. "Morphology and Ultrastructure of Prismatic Calcified Cartilage." *Microscopy and Microanalysis* 11: 1196–1197.

Martin, R. B., D. B. Burr, and N. A. Sharkey. 1998. *Skeletal Tissue Mechanics*. New York, Springer, 148–156.

Morse, P. E., M. K. Stock, K. C. James, L. J. Natanson, and S. R. Stock. 2022. "Shark Vertebral Microanatomy and Mineral Density Variation Studied with Laboratory Microcomputed Tomography." *Journal of Structural Biology* 214: 107831.

Park, J.-S., J. D. Almer, K. C. James, L. J. Natanson, and S. R. Stock. 2022a. "Mineral in Shark Vertebrae Studied by Wide Angle and by Small Angle X-Ray Scattering." *Journal of the Roy Society Interface* 19: 20220373.

Park, J.-S., H. Chen, K. C. James, L. J. Natanson, and S. R. Stock. 2022b. "Three-Dimensional Mapping of Mineral in Intact Shark Centra with Energy Dispersive X-Ray Diffraction." *Journal of the Mechanical Behavior of Biomedical Materials* 136: 105506.

Porter, M. E., and J. H. Long, Jr. 2010. "Vertebrae in Compression: Mechanical Behavior of Arches and Centra in the Gray Smooth-Hound Shark (*Mustelus californicus*)." *Journal of Morphology* 271: 366–375.

Porter, M. E., C. Diaz, J. J. Sturm, S. Grotmol, A. P. Summers, and J. H. Long, Jr. 2014. "Built for Speed: Strain in the Cartilaginous Vertebral Columns of Sharks." *Zoology* 117: 19–27.

https://doi.org/10.1017/S0885715624000307 Published online by Cambridge University Press

Stock, S. R., F. DeCarlo, and J. D. Almer. 2008. "High Energy X-Ray Scattering Tomography Applied to Bone." *Journal of Structural Biology* 161: 144–150.

Stock, S. R., J.-S. Park, A. Jakus, M. Birkbak, S. Frølich, H. Birkedal, R. Shah, and J. D. Almer. 2021. "In Situ Loading and X-Ray Diffraction Quantification of Strains in Hydroxyapatite Particles Within a 3D Printed Scaffold." *Materialia* 18: 101174.

Stock, S. R., P. E. Morse, M. K. Stock, K. C. James, L. J. Natanson, H. Chen, P. D. Shevchenko, E. R. Maxey, O. Antipova, and J.-S. Park. 2022. "Microstructure and Energy Dispersive Diffraction Reconstruction of 3D Patterns of Crystallographic Texture in a Shark Centrum." *Journal of Medical Imaging* 9: 031504.

Urist, M. R. 1961. "Calcium and Phosphorus in the Blood and Skeleton of the Elasmobranchii." *Endocrinology* 69: 778–801.

Watanabe, Y. Y., C. Lydersen, A. T. Fisk, and K. M. Kovacs. 2012. "The Slowest Fish: Swim Speed and Tail-Beat Frequency of Greenland Sharks." *Journal of Experimental Marine Biology and Ecology* 426/427: 5–11.

Weidner, D. J., M. T. Vaughan, L. Wang, H. Long, L. Li, N. A. Dixon, and W. B. Durham. 2010. "Precise Stress Measurements with White Synchrotron X-Rays." *Review of Scientific Instruments* 81: 013903.

https://doi.org/10.1017/S0885715624000307 Published online by Cambridge University Press